Gu, Chao; Lian, Junhe; Bao, Yanping; Münstermann, Sebastian

Microstructure-based fatigue modelling with residual stresses: Prediction of the microcrack initiation around inclusions

Published in:
Materials Science and Engineering A

DOI:
10.1016/j.msea.2019.02.058

Published: 28/03/2019

Document Version
Peer reviewed version

Microstructure-based fatigue modelling with residual stresses: prediction of the microcrack initiation around inclusions

Chao Gu[a,d], Junhe Lian[b,c*], Yanping Bao[a*], Sebastian Münstermann[d]

[a] *State Key Laboratory of Advanced Metallurgy, University of Science and Technology Beijing, Beijing 100083, PR China*

[b] *Department of Mechanical Engineering, Aalto University, Puumiehenkuja 3, 02150 Espoo, Finland*

[c] *Impact and Crashworthiness Lab, Department of Mechanical Engineering, Massachusetts Institute of Technology, 77 Massachusetts Avenue, Cambridge, MA 02139-4307, USA*

[d] *Steel Institute, RWTH Aachen University, Intzestraße 1, Aachen 52074, Germany*

[*] Corresponding author.

E-mail address: junhe.lian@aalto.fi (J. Lian); baoyp@ustb.edu.cn (Y. Bao)

Abstract: In the investigation of fatigue properties of metals, the microstructure-based modelling has shown its powerful applicability in predicting the microcrack initiation as well as the fatigue life. However, proper treatment of the inclusions, which are the major fatigue crack trigger especially for the very high cycle fatigue regime, is still missing. It is emphasised that in addition to the geometrical representation and the basic mechanical properties assignment of the inclusions, the residual stresses developed between the steel matrix and inclusions during the cooling processes due to their distinct thermal expansion coefficients play a non-negligible role in determining the fatigue properties. Therefore, it is aimed, in this study, to propose a microstructure-based modelling approach to account for the effects of residual stresses induced by the rapid cooling process on the fatigue crack initiation behaviour of a martensitic steel, for which the majority of the fatigue crack is formed around the calcium aluminate inclusions in experiments. The entire approach is decomposed into two processes: i) simulation of the cooling process to obtain the residual stress profile around the inclusion and ii) conducting the fatigue simulation using a crystal plasticity model including the mapped residual stress profile from the previous step. It is shown that the proposed approach accurately predicts the fatigue crack initiation sites around the inclusions corresponding to the experimental findings, while the modelling approach without the residual stresses fails to predict the correct locations of the crack initiation, revealing the necessity to consider the residual stresses for the future fatigue modelling and assessment.

Keywords: Microstructure-sensitive modelling; Crystal plasticity; Representative volume element, Very high cycle fatigue; Martensitic steels

Citation:
Gu, C., Lian, J., Bao, Y., Münstermann, S., 2019. Microstructure-based fatigue modelling with residual stresses: Prediction of the microcrack initiation around inclusions. Materials Science and Engineering: A 751, 133-141. https://doi.org/10.1016/j.msea.2019.02.058.

1. Introduction

Fatigue behaviour is an important mechanical property for many kinds of materials, especially for those used in the safety-relevant parts of engineering structures in various industrial sectors, e.g. automotive, aerospace, and railroad, etc. To ensure the reliability and safety of these facilities, the demand on the fatigue life of materials has been steadily increased. Subsequently, extensive studies have been conducted on the identification of fatigue mechanisms for various steels. Lankford and Kusenberger [1] found that crack initiation accounts for a significant portion of fatigue life in steels. Lu et al. [2] represented three kinds of failure modes of a bearing steel during fatigue tests: surface crack mode, internal crack mode without fine granular area (FGA) and internal crack mode with FGA which is usually generated around inclusions, and attributed the scatter of fatigue life to the scatter of the inclusion size. For high cycle fatigue (HCF) and very high cycle fatigue (VHCF) loading, the FGA structure is usually generated around internal crack initiation sites and the diameter of FGA corresponds to the threshold size of crack propagation [3]. Hong et al. [4] claimed that the formation of FGA is caused by numerous cyclic pressing between originated crack surfaces, resulting in grain refinement around the originated crack. Diving to the governing features of the fatigue life, roughness is considered to be the main player for the surface fatigue failure type [5]; while for internal fatigue failure, the key parameters are the size of the crack initiating discontinuity and the inclusion depth from inclusion centre to the surface to specimen and the crack initiating failure type [6]. All these studies on fatigue mechanisms conclude that the dominant factors for the fatigue life include the extrinsic features, e.g. surface roughness, and intrinsic microstructural features, e.g. texture inhomogeneity and inclusions, etc. Among these competing fatigue mechanisms [7, 8], it is concluded by Li et al. [9] that the inclusion induced fatigue failure has a dominant fraction for the VHCF regime compared to the HCF one.

While there exists a wide range of experimental evidence for the influence of microstructure on the fatigue life of components, up to the recent decade, only some attempts have been made by using the numerical modelling approach. Dunne et al. [10] modelled the micro-crack nucleation and early crack growth [11] based on the theory that was derived by Mughrabi et al. [12] in the investigation of the role of persistent slip bands and various dislocation structures on the mechanism of fatigue at a microscopic scale. MacDowell and Dunne [13] further extended the study and formulated a microscopic simulation approach to quantify the influence of microstructure from the perspective of a frequency distribution of driving forces within grains of a polycrystalline ensemble, which is characterised as the microstructure-sensitive modelling approach.

The main constituents in the microstructure-sensitive simulations are the material constitutive model and the representation of the microstructure. For the material constitutive model, the crystal plasticity (CP) model is used to calculate dislocation reactions on the slip systems. The initial crystal plasticity model was developed simply to accommodate the slip deformation in a single crystal [14]. Consideration of polycrystalline features, such as texture, has increased the applicability of crystal plasticity models to address questions at a microstructural level [15-18]. Furthermore, strain-gradient considerations were implemented to introduce size effects [19, 20], and dislocation density based laws were incorporated instead of the phenomenological description of slipping [21]. The latter developments also included grain boundary mechanisms [22-25] and damage initiation [26].

For the representation of the microstructure, the most straightforward approach is the immediate mapping of a micrograph in a geometric finite element mesh [27]. As a benefit, the calculation leads to matching the simulation and experimental results [28]. However, the simulated

material behaviour is restricted to the instantly mapped area. Alternatively, statistical-based synthetic microstructure [29-31] models are also used to represent the microstructure features. This approach usually employs the statistical information gathered from micrographs, such as the phase fraction and grain size distribution [32]. The information is further processed with mathematic models to transfer into a representative volume elements (RVE) model. Although such an artificial representative microstructure is very unlikely to be found in real micrographs, the representativeness of the mean material properties is given for the continuum and it provides a toolkit for the microstructure sensitivity study in the microstructure design processes.

The modelling approach using these two constituents has been applied to many studies correlating the microstructure features and the mechanical properties, such as the anisotropic plasticity [33-35], ductile damage initiation behaviour [36, 37] and the grain-level residual stresses by mechanical loading [38, 39]. Concerning the recent microstructure-sensitive modelling activities of the fatigue properties, Brückner-Foit and Huang [40] simulated the micro-crack initiation of martensitic steel under cyclic loading. In this study, a simple RVE of polycrystals was generated using a Voronoi tessellation and elastic orthotropic material behaviour was assumed. Furthermore, Prasannavenkatesan et al. [41] studied the sensitivity of high cycle fatigue resistance of secondary hardening martensitic gear steels to variability in primary inclusions and pores with 3D models neglecting phase and grain properties of steel. Recently, Gillner and Münstermann [42] employed the numerical approach to link the microstructure features with the S-N curves with the assistant of RVE and crystal plasticity (CP) model.

These aforementioned studies showed the powerful applicability of the microstructure-sensitive modelling approach. However, they are all missing one important microstructural feature, which is the inclusion that accounts for the major fatigue failure for the VHCF regime. In addition, it is also noted that only a geometrical implementation of the inclusions into the RVE model with certain mechanical properties is not sufficient to represent the necessary influence of the inclusions on the fatigue property [43]. As steels, especially the martensitic steels, are often subjected to a long production process with a large range of temperature change within short time, a significant amount of residual stress could be generated around the inclusions during the cooling processes due to their different thermal expansion coefficients compared to the steel matrix. Brooksbank [44] and Ma [45] showed by modelling and analytical calculation that the type and the magnitude of the residual stress depend on the inclusions size, type, and shape. Therefore, besides the geometrical and mechanical inhomogeneity induced by the inclusions, the residual stresses also have a significant impact on the fatigue life behaviour of the materials. However, it is not yet considered in any microstructure-sensitive modelling approach due to its complication involving a multiphasic formulation of the constitute model dealing with thermal and mechanical loading. Therefore, it is aimed in this study to propose a straightforward microstructure-sensitive approach to account for the effects of residual stresses induced by the rapid cooling process on the fatigue behaviour of martensitic steels.

The entire approach is decomposed into two processes: i) simulation of the cooling process to obtain the residual stress profile around the inclusion and ii) conducting the fatigue simulation using a crystal plasticity model with the mapped residual stress profile from the previous step. In the following sections, these relevant procedures will be given in detail. In section 2, the experimental methods are described for the microstructure characterisation as well as for the mechanical testing. The description of the modelling scheme will be followed in section 3, covering the RVE model generation algorithm, the cooling, and fatigue simulation. In section 4, both the experimental and

numerical results are presented. For the fatigue simulation, both simulations with and without the residual stress profile are compared and discussed. The concluding remarks are drawn in section 5.

2. Material and experiments

2.1 Material

The material in this investigation is a high-carbon chromium-bearing steel, GB GCr15 (equivalent to SAE 52100). The main composition is shown in **Table 1**. Heat treatment procedures consist of annealing, vacuum oil quenching after holding for 20 min at 835°C, and tempering. The tempering condition was maintained for 120 min at 180°C.

Table 1 Chemical composition (unit: weight %).

C	Cr	Si	Mn	P	S	Cu	Al
1.03	1.37	0.21	0.33	0.0110	0.0008	0.0744	0.0110

2.2 Experiments

Electron backscatter diffraction (EBSD) was conducted for the analysis of the microstructure of CCr15. To obtain the representative information of the statistical microstructure features, a relatively large area was measured (100×100 μm^2). The step size was set as 50 nm to be able to capture the details of the microstructure.

The HCF and VHCF tests were used to analyse the fatigue property of the materials with a frequency of 20 kHz, while the LCF was conducted to calibrate the material parameters for the crystal plasticity model with a frequency of 0.01 Hz. The loading condition of all the tests was a fully reversed tension-compression ($R = -1$). The specimen shapes are shown in **Fig. 2**. The arc part in the middle of the specimen was polished. The polished scratches were all in the longitudinal direction so that the probability of crack initiation caused by surface defects was minimized.

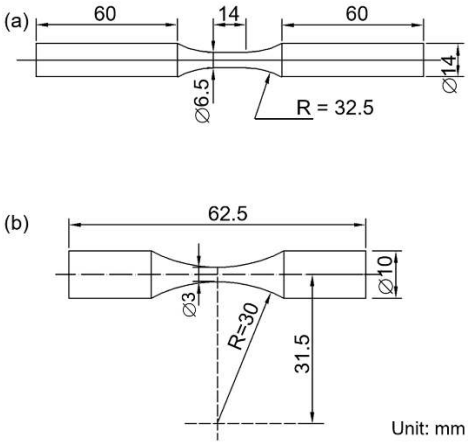

Fig. 2. Specimen geometry and dimensions for: (a) HCF and VHCF test; (b) LCF test.

The strain of LCF test was kept constant at 1.1% and 1.2%. The frequency of the LCF test is 0.01 Hz. The VHCF test was performed under a resonance frequency of 20 kHz. During the test, the temperature of the specimen was kept under 50°C by air cooling. After the VHCF test, the fracture surfaces were qualitatively assessed with scanning electron microscopy (SEM). The composition around crack initiation sites was analysed by energy dispersive spectrometer (EDS) to

identify the fatigue initiation mechanism.

3. Modelling scheme

3.1 RVE generation

3.1.1 Steel matrix

Based on the result of EBSD analysis, the grain-level information can be quantified and it was prepared as an input for the RVE generation of the steel matrix. These two-dimensional microstructure models were generated by a well-developed MATLAB code and Python scripts for the finite element (FE) software Abaqus. The generation obeyed the random sequential addition (RSA) algorithm [46] and Voronoi tessellation technique. The centre of each grain was firstly predefined as Voronoi seed. The grain size was assigned to the tessellation algorithm as the weight of its seed. The number of grain generated in the model area was determined by the relation of the area distribution of a list of virtual circles to the desired grain size distribution. Thereafter, the RSA algorithm was applied to arrange all the circles in the model area and none of each was allowed to overlap. Then the grains were created accordingly. The periodicity of the microstructure was also ensured. The readers are referred to previous studies [32, 42], where the generation method was reported in detail.

3.1.2 Inclusions

For inclusions, the real geometry was used. The input was obtained by the SEM micrograph of the fracture surface, where inclusions were triggering the fatigue failure. The graph was further processed by MATLAB to obtain the digitalised coordinates of the inclusion geometries, which were then implemented into the RVE generated in the previous step for the matrix representation. For simplicity, the inclusions were placed at the centre of the RVE.

3.2 Residual stress simulation during the cooling process

The residual stress simulation was based on the RVE generated from the previous step. The simulation was conducted in Abaqus/Standard and the mechanical properties of both the inclusion and the matrix are assumed to be isotropic and elastic only. During fast cooling of steels, residual stresses will be generated between the inclusion and the steel matrix due to the different expansion coefficients. In this model, the cooling process during quenching (temperature variation from 835°C to 20°C) was taken into consideration while the tempering process was overlooked due to its relatively minor effect on the residual stress reduction. The mechanical properties and the thermal expansion coefficient of calcium aluminate inclusion, which is identified as the main fatigue trigger for the investigated steel in section 4, and matrix are shown in **Table 2** [44, 47]. For more details of the residual stress simulation and its application to other major inclusion types, readers are referred to Gu et al. [48]. The obtained residual stress profile in terms of full stress tensor is further element-to-element mapped to the fatigue simulation model.

Table 2 Mechanical and thermal properties of the inclusion and steel matrix.

Material	Coefficient of thermal expansion, α (10^{-6}/°C)	Young's modulus, E (GPa)	Poisson's ratio, v
Inclusion	5.0	113	0.234
Matrix	23.0	210	0.300

3.3 Crystal plasticity model for the steel matrix

The mechanical behaviour of the steel matrix under cyclic loading was rendered by the crystal plasticity model. The formulation of the model is based on the well-established phenomenological description of slip, which can be found in detail in the review paper by Roters et al. [49]. The model was extended to include the kinematic hardening in our previous study [42]. For the completeness of the modelling scheme, the main equations of the model are briefly introduced below.

The deformation gradient **F** consists of an elastic part and a plastic part:

$$\mathbf{F} = \mathbf{F}_\mathrm{e}\mathbf{F}_\mathrm{p}, \tag{1}$$

where $\mathbf{F}_\mathrm{e}$ represents the elastic deformation gradient and $\mathbf{F}_\mathrm{p}$ represents the plastic deformation gradient. The elastic deformation includes small lattice deformation and large rigid body rotation and the plastic deformation is the irreversible deformation after the forces and displacements are removed.

The rate of the plastic deformation gradient $\dot{\mathbf{F}}_\mathrm{p}$ can be calculated by Eq. (2):

$$\dot{\mathbf{F}}_\mathrm{p} = \mathbf{L}_\mathrm{p}\mathbf{F}_\mathrm{p}, \tag{2}$$

where $\mathbf{L}_\mathrm{p}$ is the plastic velocity gradient, which can be expressed by Eq. (3) [50]:

$$\mathbf{L}_\mathrm{p} = \dot{\mathbf{F}}_\mathrm{p}\mathbf{F}_\mathrm{p}^{-1}., \tag{3}$$

Based on the assumption that the dislocation slip is responsible for plastic deformation, the plastic velocity gradient $\mathbf{L}_\mathrm{p}$ can be expressed as the sum of all shear rates on the slip systems:

$$\mathbf{L}_\mathrm{p} = \sum_{\alpha=1}^{N} \dot{\gamma}^\alpha \mathbf{S}^\alpha, \tag{4}$$

where N is the total number of active slip systems; $\dot{\gamma}^\alpha$ is the shear rate on the slip system α and $\mathbf{S}^\alpha$ is the Schmid tensor of the slip system α, which can be expressed by Eq. (5):

$$\mathbf{S}^\alpha = \mathbf{m}^\alpha \otimes \mathbf{n}^\alpha, \tag{5}$$

where $\mathbf{m}^\alpha$ and $\mathbf{n}^\alpha$ are the slip direction and plane normal vectors of the slip system α.

The shear rate $\dot{\gamma}^\alpha$ is a function of the resolved shear stress τ^α and the critical resolved shear stress τ_c^α:

$$\dot{\gamma}^\alpha = f(\tau^\alpha, \tau_c^\alpha), \tag{6}$$

The resolved shear stress τ^α is expressed as:

$$\tau^\alpha = \mathbf{S} \cdot \mathbf{S}^\alpha, \tag{7}$$

where $\mathbf{S}$ is the second Piola-Kirchhoff stress. The shear rate can be then expressed:

$$\dot{\gamma}^\alpha = \dot{\gamma}_0 \left|\frac{\tau^\alpha - \chi^\alpha}{\tau_\mathrm{c}^\alpha}\right|^{\frac{1}{m}} \mathrm{sgn}(\tau^\alpha - \chi^\alpha), \tag{8}$$

where $\dot{\gamma}_0$ is the initial slip rate; m is the strain rate sensitivity factor and χ^α is the kinematic back stress on slip system α. A nonlinear kinematic hardening rule initially proposed by Armstrong and Frederick [51] was implemented for fatigue analysis [51]:

$$\dot{\chi}^\alpha = G_1\dot{\gamma}^\alpha - G_2|\dot{\gamma}^\alpha|\chi^\alpha, \tag{9}$$

where χ^α is the back stress of slip system α; G_1 and G_2 are material parameters, which need to be calibrated.

The micromechanical interaction among different slip systems is empirically captured by the hardening evolution law of the slip system α:

$$\tau_c^\alpha = \tau_0 + \sum_{\beta=1}^{N} h_{\alpha\beta}\left|\Delta\gamma^\beta\right|, \tag{10}$$

where τ_0 is the initial resolved shear stress; $\Delta\gamma^\beta$ is the plastic slip increment of each slip system β and $h_{\alpha\beta}$ is referred to as the hardening matrix:

$$h_{\alpha\beta} = q_{\alpha\beta}\left[h_0\left(1 - \frac{\tau_\mathrm{c}^\beta}{\tau_\mathrm{c}^\mathrm{s}}\right)^a\right], \tag{11}$$

where $q_{\alpha\beta}$ is a measure for self-hardening and latent hardening. Its value is taken as 1.0 for

coplanar slip systems and 1.4 otherwise. The rest parameters h_0, τ_c^s, and a are hardening parameters.

The calibration of parameters in the crystal plasticity model is conducted with an iterative fitting of the RVE simulation to the hysteresis loops obtained from LCF tests with strain amplitudes of 1.1% and 1.2%. For both strain amplitudes, the stable stress–strain cycles were taken. The parameters to be calibrated are τ_0, τ_c^s, h_0, a, $\dot{\gamma}_0$, m, G_1, G_2 and elastic parameters C_{11}, C_{12} and C_{44}. The calibration of these parameters is described in chapter 4.2.2.

The aforementioned model was implemented in Abaqus/Standard as a user subroutine (UMAT). The purpose of this model is to calculate the stress required to reach the final deformation gradient and to determine the material Jacobian $\mathbf{J} = \partial\Delta\boldsymbol{\sigma}/\partial\Delta\boldsymbol{\varepsilon}$ for the iterative procedure by perturbation methods. The stress calculation was implemented using the typical predictor-corrector method based on the Newton–Raphson scheme.

4. Results and discussion

4.1 Microstructure analysis

The EBSD of the inverse pole figure on the cross-section of the steel bar is presented in **Fig. 3**. The results show that the investigated steel has a rather fine microstructure due to its heat treatment history. The coloured grains are the tempered martensitic packets/blocks while the black ones are mainly the fresh martensite and/or carbides. The tempered martensite is taking up most of the volume fraction of the steel (about 90%) and leaves about 10% for the rest. Due to the limited volume fraction and the very fine size of the secondary phase, which leads to minor effects on the fatigue failure mechanisms as identified in the following section, only the tempered martensite was considered in the following RVE construction for the steel matrix.

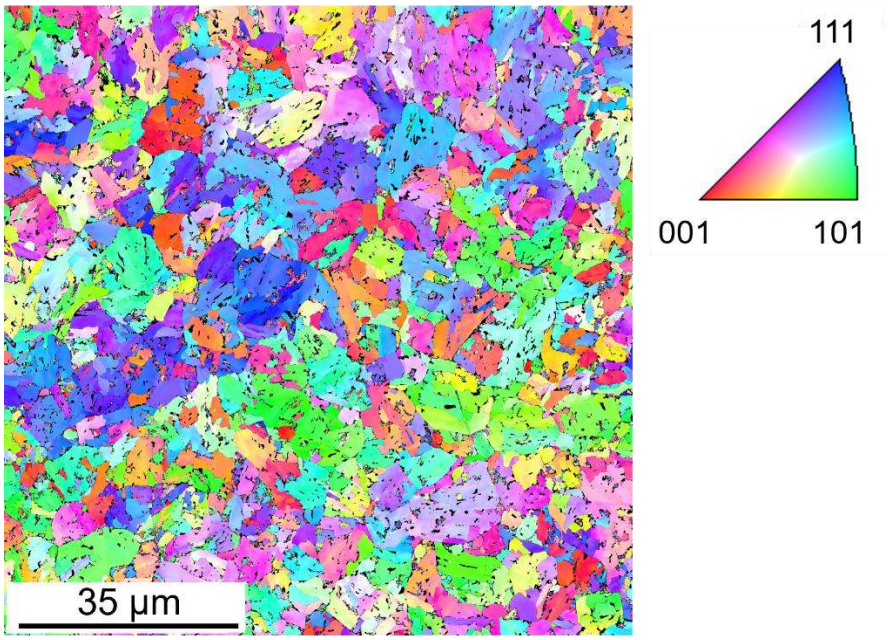

Fig. 3. The EBSD graph of the inverse pole figure on the cross section of steel bar.

4.2 Fatigue crack initiation analysis

The fatigue failure in HCF and VHCF regimes in the present study all initiated due to inner

cracks, among which, 65% of the cracks were initiated around inclusions. The morphologies and compositions of the inclusions at the crack initiation sites were analysed. There are three main types of inclusions causing the crack: spherical calcium aluminate, titanium nitride, and spinel, which are common inclusions in steels [52, 53]. The ratio of fatigue failure sorted by crack initiation mechanisms is shown in **Fig. 4.** Spherical calcium aluminates contribute the most to the fatigue crack initiation. The typical morphology and EDS results of a typical crack initiation site with a spherical calcium aluminate inclusion are shown in **Fig. 5 (a)** and **(b)**. Therefore, in the following numerical study concerning the residual stress analysis and the fatigue simulation, only the calcium aluminates are considered.

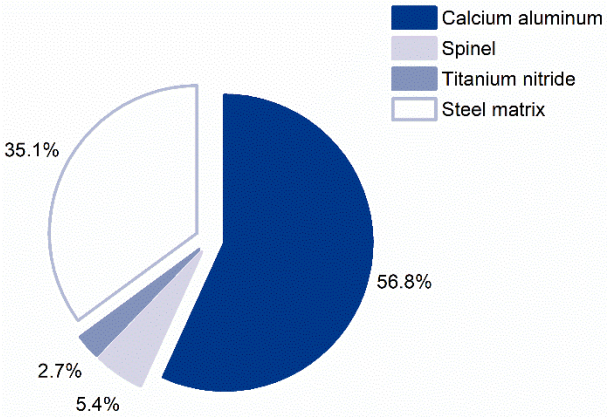

Fig. 4. The ratio of fatigue failure sorted by crack initiation mechanisms.

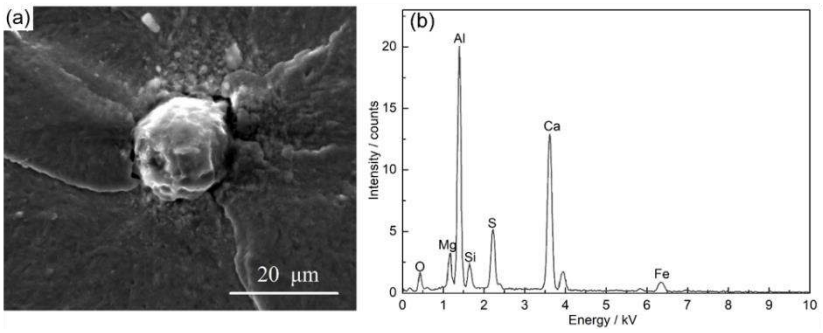

Fig. 5. A typical fatigue initiation site with a spherical calcium aluminate inclusion: (a) SEM micrograph; (b) the composition of the inclusion [54].

4.3 Modelling of steel matrix

4.3.1 Statistical virtual microstructure

For the quantitative analysis of the grain size distribution of the tempered martensite, the following log-normal distribution density function is used:

$$y = f(x|\mu,\sigma) = \frac{1}{x\sigma\sqrt{2\pi}}\exp\left(\frac{-(\ln x-\mu)^2}{2\sigma^2}\right) \tag{12}$$

where μ is the mean value; σ is the standard deviation, while x and y are the grain size and the frequency, respectively.

The fitted distribution density function and the parameters are shown in **Fig. 6**(a), which were used as an input for RVE generation. These two-dimensional microstructure models were generated

according to the aforementioned algorithm and imported into the finite element software Abaqus. The position of each grain was random in the model area. In this study, 60 RVEs were generated. These RVEs have periodic microstructures with a size of 70 × 70 μm^2. Each RVE contains approximately 200 grains, see **Fig. 6**(b), which are enough to ensure a reliable result according to the study by Fritzen et al. [55] and Cailletaud et al. [56].

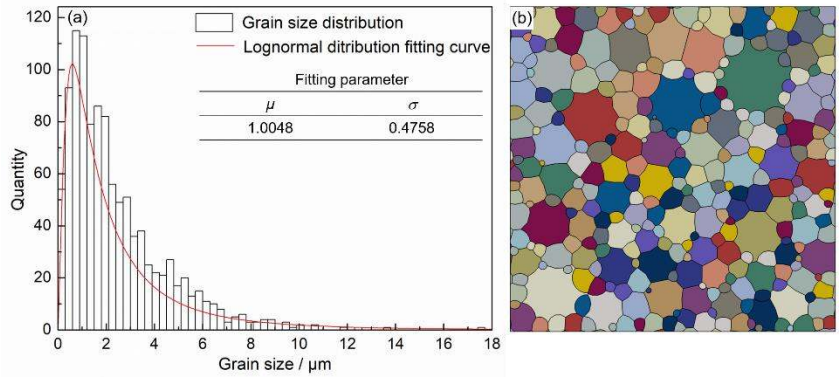

Fig. 6. (a) Grain size distribution of the investigated steel GCr15 and the log-normal fitting parameters; (b) virtual microstructure of the investigated steel based on the fitting parameters in Fig. 6(a).

4.3.2 Parameters calibration of the crystal plasticity model

To simulate the response behaviour of the steel matrix on stress, CP parameters described in Section 3.3 were fitted. The fitting was conducted with the LCF results. The hysteresis loops are not stable during the first 10 cycles according to the LCF results. As a result, the following stable hysteresis loops were chosen for the iterative fitting with the trial and error method. The fitting simulation was conducted under the same frequency with LCF tests. The fitting results and parameters are shown in **Fig. 7** and **Table 3**.

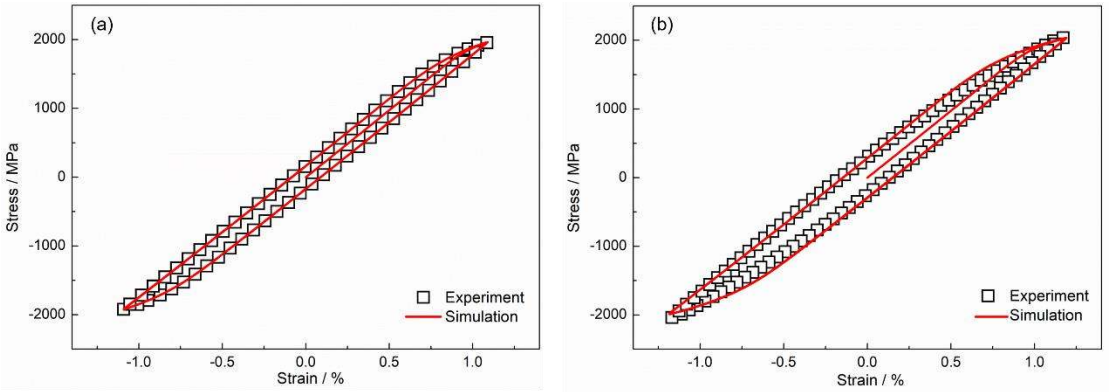

Fig. 7. Parameter calibration of the CP model based on the experimental and numerical results on the hysteresis loops: (a) strain 1.1%; (b) strain 1.2%.

Table 3 CP model fitting parameter.

C_{11}: 193.9 GPa	C_{12}: 94.6 GPa	C_{44}: 92.2 GPa	$\dot{\gamma}_0$: 0.01
$1/m$: 100	τ_0: 645 MPa	G_1: 100000 MPa	G_2: 2000
h_0: 1000 MPa	a: 1.1	τ_c^s: 2500 MPa	

4.4 Modelling of inclusions

The geometrical shape of the inclusion shown in Fig. 5 was digitalized and inserted into all 60 RVEs. **Fig. 8** shows nine examples of the RVEs with the inclusion of dark grey colour in the centre. The virtual microstructures differ from each other in the nine RVEs, while the geometry and position of the inclusion remain consistent. It is noted that the inclusions are perfectly bonded with the steel matrix and the geometrical/mechanical properties of the bonding layers are omitted in this study. The 60 RVEs with inclusions are firstly subjected to the cooling simulation to qualify the residual stresses. As shown in Fig. 8, with different matrix around the inclusion in the nine RVEs, the residual stress distribution appears only minor changes. The residual stresses around the inclusion increase with the decrease of the distance to the boundary between inclusion and steel matrix and peak on the boundary, which is consistent with the calculation results with models of Brooksbank and Andrews [44]. The high residual stresses on the boundary around a single inclusion also vary in terms of different local shapes of the inclusion. The larger the local curvature of inclusion edge is, the larger the residual stress is. When inclusions are considered in the simulation process, residual stress distribution will contribute to the fatigue life.

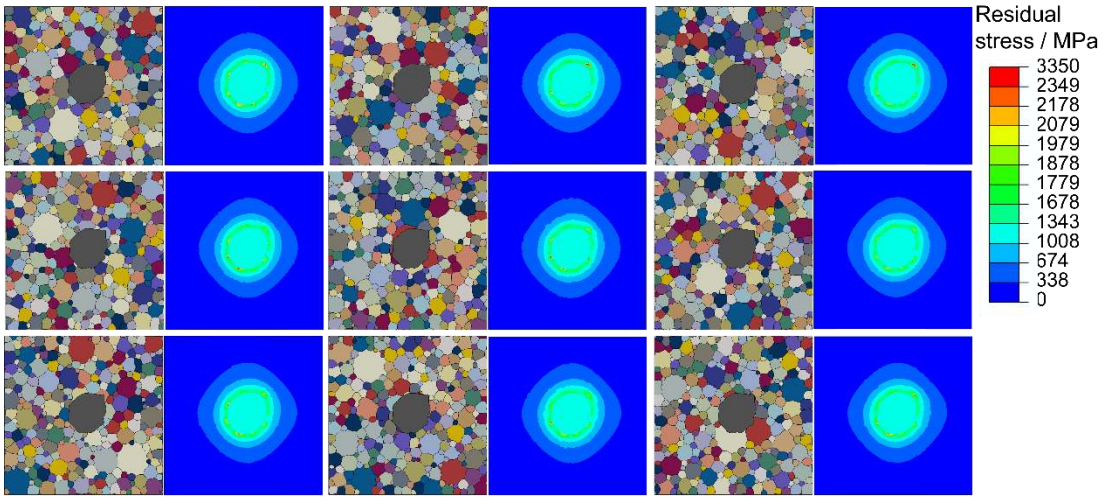

Fig. 8. Nine different RVEs of virtue martensitic microstructure with the same geometry of the inclusion shown in Fig. 5(a) in the centre and the corresponding residual stress distributions after the cooling simulation.

4.5 Fatigue simulation and fatigue indicator parameter implementation

The accumulated plastic slip or the plastic strain on the macroscopic level is generally considered to be the indicator of the crack initiation for various failure types. For ductile fracture, many experimental and numerical studies indicated that the crack initiation position is not only dependent on the plastic strain accumulation but also the local stress state, i.e. stress triaxiality and Lode angle, which formulates a stress-state-dependent plastic strain indicator [57-60]. For the microscopic fatigue mechanism, according to the studies of Mughrabi et al. [11, 61], Dunne et al. [10], Manonukul and Dunne [62] and Cheong and Busso [63], the accumulated plastic slip is considered to be the major crack initiation indicator on the microscopic level. It can lead to different incompatible shape changes of neighbouring grains, which impels intergranular crack initiation. Larger accumulated dislocation slip suggests a higher possibility of fatigue crack initiation. In addition, the accumulated dislocation slip is also proven by Mughrabi and Wüthrich [64] and

Sommer et al. [65] to be quantitatively related to fatigue life.

In this study, the local accumulated dislocation slip is qualitatively recognized as the fatigue crack indicator. The position of the maximum value of local accumulated dislocation slip is identified as the crack initiation site on the investigated area. In terms of the plastic velocity gradient, the local accumulated dislocation slip p_{acc} can be calculated with Eq. (13).

$$p_{\mathrm{acc}} = \int_0^t \sqrt{\frac{2}{3}\boldsymbol{L}_{\mathrm{p}} : \boldsymbol{L}_{\mathrm{p}}}\, dt \tag{13}$$

During the fatigue simulation process, a pre-defined stress magnitude of 1250 MPa was applied. The simulation also applied a fully reversed tension-compression ($R = -1$) under a frequency of 20 kHz. According to previous studies [42, 66], the increase of p_{acc} at the critical location shows a proportional relation with respect to the cycle number. Therefore, the number of cycles can be any number larger than two for capturing the statistical distribution of the development of p_{acc} in different RVEs. In the present study, six cycles were simulated during the fatigue process. After six cycles of simulation, the values of p_{acc} in 60 RVEs were calculated with the models neglecting residual stress and considering residual stress. The p_{acc} distributions on the nine RVEs shown in Fig. 8 are presented in **Fig. 9** (neglecting residual stresses) and **Fig. 10** (considering residual stresses). The values of p_{acc} in **Fig. 10** show different distributions and obviously larger values compared to the values in **Fig. 9**, which is caused by the residual stress.

However, due to the meshing effects in FE modelling, it is not convenient to discuss the fatigue behaviour with the local p_{acc}. In the present study, the maximum grain-level averaged value P_{max} is introduced to identify the precursor of fatigue crack nucleation, which is the maximum value of the total sum of p_{acc} in all finite elements of a single grain divided by the grain volume, see Eq. (14).

$$P_{\mathrm{max}} = \max\left(\frac{1}{\sum_{i=1}^{N_{\mathrm{E}}^{\mathrm{Gr}}} V_i^{\mathrm{Gr}}} \sum_{i=1}^{N_{\mathrm{E}}^{\mathrm{Gr}}} p_i\, V_i^{\mathrm{Gr}}\right), \tag{14}$$

where the parameter i is the identifier of the finite element of the involved grain, $N_{\mathrm{E}}^{\mathrm{Gr}}$ is the number of elements within the grain, and V_i^{Gr} is the volume of the element i of the grain.

In **Fig. 9** and **Fig. 10**, the positions of P_{max} are pointed out by the white arrows, which demonstrate the fatigue crack initiation sites. When the residual stresses are considered, the locations of P_{max} in nine RVEs are around the inclusion, indicating the crack initiation sites are correctly predicted. In contrast, when the residual stresses are neglected, only a few crack initiation sites, e.g. **Fig. 9**(c), (d), (f) and (i), are located around the inclusion.

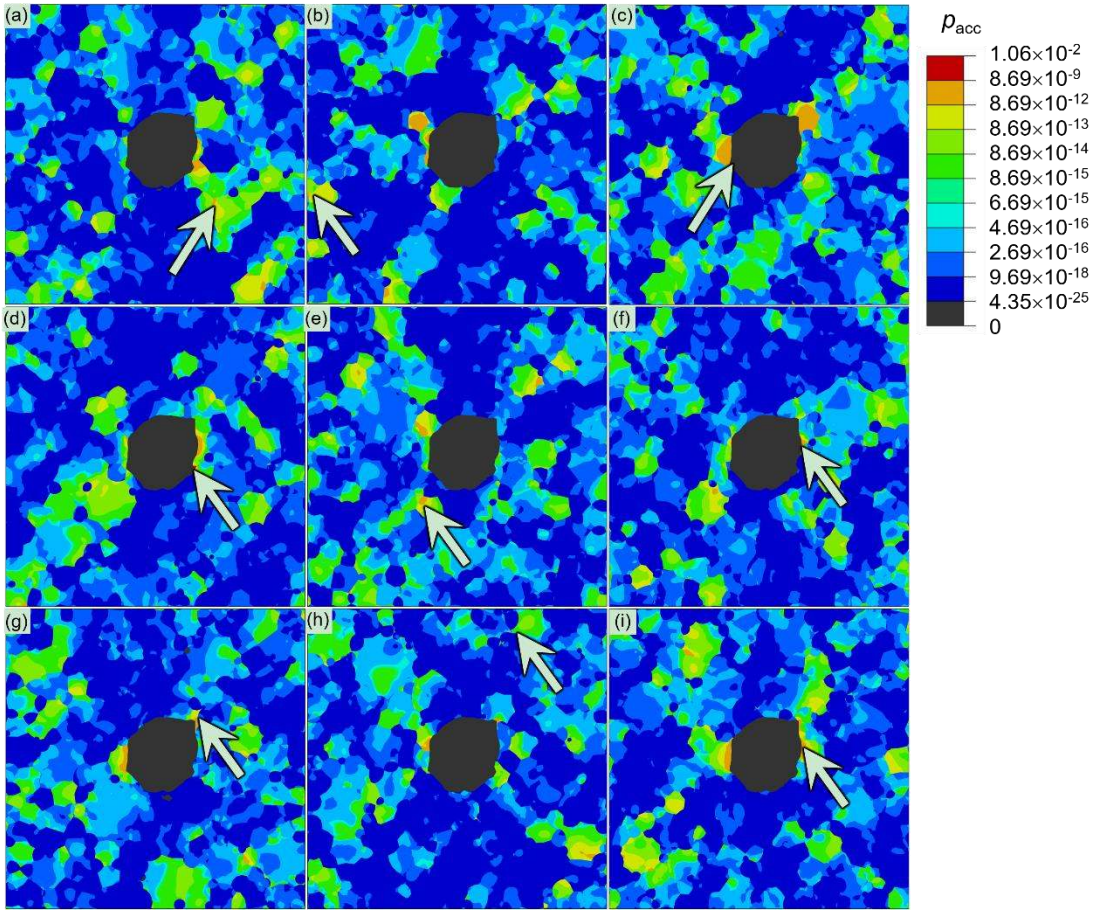

Fig. 9. The p_{acc} contour distribution of steel matrix in nine typical RVEs after six-cycle simulation of tension-compression fatigue stress neglecting the residual stress generated during the cooling process.

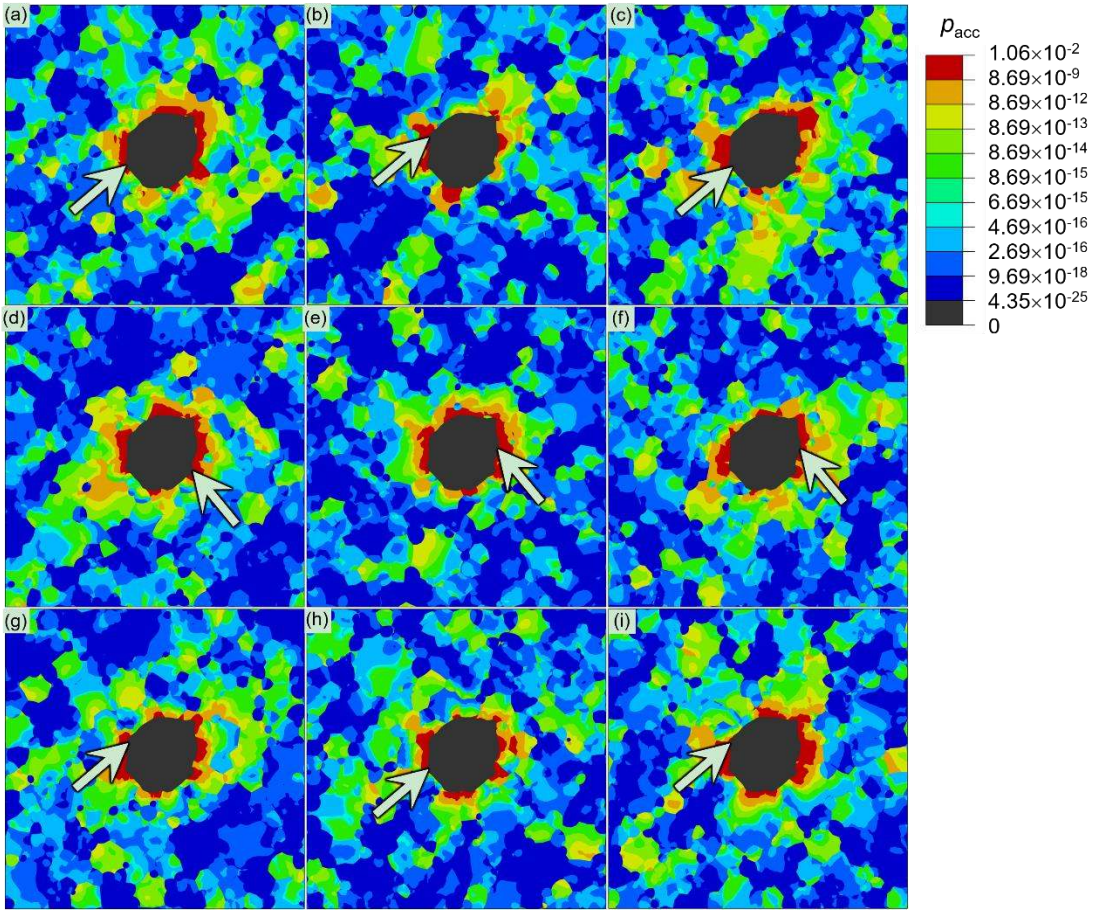

Fig. 10. The p_{acc} contour distribution of steel matrix in nine typical RVEs after six-cycle simulation of tension-compression fatigue stress considering the residual stress generated during the cooling process.

To clarify the effect of residual stresses on the accumulated dislocation slip, the history of local stress and p_{acc} on the crack initiation point in a RVE by models considering and neglecting residual stress are extracted. The local point for data extraction is chosen as the crack initiation sites shown in **Fig. 10**(d). To compare with the simulation results without considering residual stresses, the same position in **Fig. 9**(d) is also extracted. The results are presented in **Fig. 11**. The blue line represents p_{acc}. The solid red lines represent tension, while the dashed red lines represent compression. For the simulation without residual stresses, the local stress starts from zero. When tension and compression are applied during the first and third quarter of a single cycle, the local stress increases. During the process of unloading in the second and fourth quarter of the cycle, the local stress goes back to zero. When the local stress increases to a value that triggers the plastic deformation, p_{acc} gets accumulated.

When residual stress is considered, the local residual stress value is the initial status of the investigated spot. The value is high and consistent with the residual stress shown in **Fig. 8**. Since the residual stress is compressive, when tension is applied during the first quarter of the cycle, an obvious stress relaxation could be observed in **Fig. 11**(b). After relaxing to a stress value close to 1250 MPa, the stress starts to increase again and then reaches a peak. The reason for this is simply related to the increase of p_{acc} of the local point. Although the stress decreases during the relaxation phase, the value of p_{acc} keeps increasing. After it reaches a value that induces the stress due to hardening, equal to the relaxed residual stress, the stress minimum appears. Further tensile loading gives rise to the significant increase of the p_{acc} due to hardening till the stress maximum at the end

of the first quarter cycle. It should be noticed that during unloading, the local stress decreased to a finite value instead of zero, and this stress remains constant after the cyclic loading. It can be referred to as the relaxed residual stress and remains compressive. The value of this stress will influence the stress and p_{acc} behaviour of the local point during the compression cycle of the loading. For the selected local point in this analysis, its value is still lower than the maximum possible compressive stress, as shown in **Fig. 11**(a). Therefore, a minor increase of the stress appears to this point. It is noted that this stress level is the same as the case neglecting the residual stress. However, the accumulation of the p_{acc} is not observed, because compared to the large extent of the tensile deformation, the resulting compressive one is negligible. It is further noticed that the accumulation of p_{acc} becomes less and less with the increase of cycle members, which is quite different from the case without residual stress. The explanation for this also lies in the kinematic hardening behaviour of the local point. For the case without the residual stress, the hardening is so small and it stays at a rather liner pattern, while for the case with residual stress, the hardening is high enough to reach the non-linear part, where the hardening rate becomes slower.

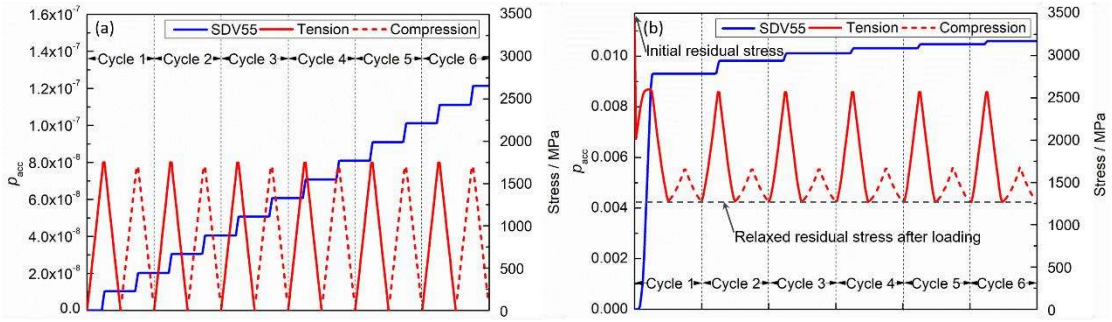

Fig. 11. Stress and p_{acc} variation with fatigue cycles: (a) without residual stress; (b) with residual stress.

5. Conclusions

In this study, the fatigue properties of a high-carbon chromium martensitic steel were investigated, and a microstructure-based model considering residual stresses induced by the rapid cooling process was built to describe the fatigue process, based on which the crack initiation sites were predicted. The following conclusions are drawn:

- For the high-carbon chromium bearing steels in the present study, most internal cracks initiate around spherical calcium aluminate inclusions for both HCF and VHCF tests.
- A microstructure-based modelling approach to account for the effects of the residual stress induced by rapid cooling processes on the fatigue behaviour is proposed.
- For the selected inclusions type, a strong compressive residual stress is induced during the rapid cooling process of the steel and local maximum is reached at the interface of the inclusion with large curvatures.
- With this approach, the predicted fatigue crack initiation sites are in a good agreement with the experimental observation, which was not the case for the modelling approach neglecting the residual stresses between the inclusions and matrix.
- The reason for the fatigue crack at the interface of inclusion and matrix is attributed to a large amount of accumulation of the plastic slip during the residual stress relaxation at the local point when the tensile loading is applied.

Acknowledgements

This work was supported by the China Scholarship Council and the State Key Laboratory for Advanced Metallurgy Foundation (No. 41602014).

References

[1] J. Lankford, F.N. Kusenberger, Initiation of fatigue cracks in 4340 steel, Metallurgical Transactions 4(2) (1973) 553-559.

[2] L.L.L.W.Z. Jiwang, S.K.Z. Weihua, Analysis of rotary bending gigacycle fatigue properties of bearing steel GCr15, Acta Metallurgica Sinica 45(1) (2009) 73-78.

[3] Y. Hong, Z. Lei, C. Sun, A. Zhao, Propensities of crack interior initiation and early growth for very-high-cycle fatigue of high strength steels, International Journal of Fatigue 58 (2014) 144-151.

[4] Y. Hong, X. Liu, Z. Lei, C. Sun, The formation mechanism of characteristic region at crack initiation for very-high-cycle fatigue of high-strength steels, International Journal of Fatigue 89 (2016) 108-118.

[5] H. Itoga, Effect of surface roughness on step-wise S–N characteristics in high strength steel, International Journal of Fatigue 25(5) (2003) 379-385.

[6] D. Krewerth, T. Lippmann, A. Weidner, H. Biermann, Influence of non-metallic inclusions on fatigue life in the very high cycle fatigue regime, International Journal of Fatigue 84 (2016) 40-52.

[7] P. Zhao, G. Gao, R.D.K. Misra, B. Bai, Effect of microstructure on the very high cycle fatigue behavior of a bainite/martensite multiphase steel, Materials Science and Engineering: A 630 (2015) 1-7.

[8] G. Gao, B. Zhang, C. Cheng, P. Zhao, H. Zhang, B. Bai, Very high cycle fatigue behaviors of bainite/martensite multiphase steel treated by quenching-partitioning-tempering process, International Journal of Fatigue 92 (2016) 203-210.

[9] S.X. Li, Y.Q. Weng, W.J. Hui, Z.G. Yang, Very high cycle fatigue properties of high strength steels-effects of nonmetallic inclusions, Metallurgical Industry Press, Beijing, 2010.

[10] F. Dunne, A. Wilkinson, R. Allen, Experimental and computational studies of low cycle fatigue crack nucleation in a polycrystal, International Journal of Plasticity 23(2) (2007) 273-295.

[11] H. Mughrabi, Microstructural fatigue mechanisms: Cyclic slip irreversibility, crack initiation, non-linear elastic damage analysis, International Journal of Fatigue 57 (2013) 2-8.

[12] H. Mughrabi, On 'multi-stage'fatigue life diagrams and the relevant life-controlling mechanisms in ultrahigh-cycle fatigue, Fatigue & Fracture of Engineering Materials & Structures 25(8-9) (2002) 755-764.

[13] D. McDowell, F. Dunne, Microstructure-sensitive computational modeling of fatigue crack formation, International Journal of Fatigue 32(9) (2010) 1521-1542.

[14] R. Becker, The effects of shear constraints on the lattice rotation of FCC crystals in (011) channel-die compression, Journal of the Mechanics and Physics of Solids 39(44) (1991) 459-476.

[15] D. Raabe, F. Roters, Using texture components in crystal plasticity finite element simulations, International Journal of Plasticity 20(3) (2004) 339-361.

[16] Z. Zhao, F. Roters, W. Mao, D. Raabe, Introduction of a texture component crystal plasticity finite element method for anisotropy simulations, Advanced Engineering Materials 3(12) (2001) 984-990.

[17] M.A. Melchior, L. Delannay, A texture discretization technique adapted to polycrystalline aggregates with non-uniform grain size, Computational Materials Science 37(4) (2006) 557-564.

[18] P. Eisenlohr, F. Roters, Selecting a set of discrete orientations for accurate texture reconstruction, Computational Materials Science 42(4) (2008) 670-678.

[19] N.A. Fleck, G.M. Muller, M.F. Ashby, J.W. Hutchinson, Strain gradient plasticity: Theory and experiment, Acta Metallurgica et Materialia 42(2) (1994) 475-487.
[20] W.D. Nix, H. Gao, Indentation size effects in crystalline materials: A law for strain gradient plasticity, Journal of the Mechanics and Physics of Solids 46(3) (1998) 411-425.
[21] A. Arsenlis, D. M. Parks, R. Becker, V. V. Bulatov, On the evolution of crystallographic dislocation density in non-homogeneously deforming crystals, Journal of the Mechanics and Physics of Solids 52(6) (2004) 1213-1246.
[22] A. Ma, F. Roters, D. Raabe, A dislocation density based constitutive model for crystal plasticity FEM including geometrically necessary dislocations, Acta Materialia 54(8) (2006) 2169-2179.
[23] A. Ma, F. Roters, D. Raabe, Studying the effect of grain boundaries in dislocation density based crystal-plasticity finite element simulations, International Journal of Solids and Structures 43(24) (2006) 7287-7303.
[24] A. Ma, F. Roters, D. Raabe, On the consideration of interactions between dislocations and grain boundaries in crystal plasticity finite element modeling – Theory, experiments, and simulations, Acta Materialia 54(8) (2006) 2181-2194.
[25] M. Knezevic, B. Drach, M. Ardeljan, I.J. Beyerlein, Three dimensional predictions of grain scale plasticity and grain boundaries using crystal plasticity finite element models, Computer Methods in Applied Mechanics and Engineering 277 (2014) 239-259.
[26] T. Bieler, P. Eisenlohr, F. Roters, D. Kumar, D. Mason, M. Crimp, D. Raabe, The role of heterogeneous deformation on damage nucleation at grain boundaries in single phase metals, International Journal of Plasticity 25(9) (2009) 1655-1683.
[27] J. Lian, H. Yang, N. Vajragupta, S. Münstermann, W. Bleck, A method to quantitatively upscale the damage initiation of dual-phase steels under various stress states from microscale to macroscale, Computational Materials Science 94 (2014) 245-257.
[28] U.A. Özden, K.P. Mingard, M. Zivcec, A. Bezold, C. Broeckmann, Mesoscopical finite element simulation of fatigue crack propagation in WC/Co-hardmetal, International Journal of Refractory Metals and Hard Materials 49 (2015) 261-267.
[29] M. Nygards, P. Gudmundson, Three-dimensional periodic Voronoi grain models and micromechanical FE-simulations of a two-phase steel, Computational Materials Science 24(4) (2002) 513-519.
[30] M. Nygards, P. Gudmundson, Micromechanical modeling of ferritic/pearlitic steels, Materials Science and Engineering: A 325(1-2) (2002) 435-443.
[31] Y.W. Zhao, R. Tryon, Automatic 3-D simulation and micro-stress distribution of polycrystalline metallic materials, Computer Methods in Applied Mechanics and Engineering 193(36-38) (2004) 3919-3934.
[32] N. Vajragupta, P. Wechsuwanmanee, J. Lian, M. Sharaf, S. Münstermann, A. Ma, A. Hartmaier, W. Bleck, The modeling scheme to evaluate the influence of microstructure features on microcrack formation of DP-steel: The artificial microstructure model and its application to predict the strain hardening behavior, Computational Materials Science 94 (2014) 198-213.
[33] H. Zhang, M. Diehl, F. Roters, D. Raabe, A virtual laboratory using high resolution crystal plasticity simulations to determine the initial yield surface for sheet metal forming operations, International Jounal Plasticity 80 (2016) 111-138.

[34] I. Tikhovskiy, D. Raabe, F. Roters, Simulation of earing of a 17% Cr stainless steel considering texture gradients, Materials Science and Engineering a-Structural Materials Properties Microstructure and Processing 488(1-2) (2008) 482-490.
[35] Q. Xie, A. Van Bael, Y.G. An, J. Lian, J.J. Sidor, Effects of the isotropic and anisotropic hardening within each grain on the evolution of the flow stress, the r-value and the deformation texture of tensile tests for AA6016 sheets, Materials Science and Engineering: A 721 (2018) 154-164.
[36] B. Wu, N. Vajragupta, J. Lian, U. Hangen, P. Wechsuwanmanee, S. Münstermann, Prediction of plasticity and damage initiation behaviour of C45E+N steel by micromechanical modelling, Materials & Design 121 (2017) 154-166.
[37] Q. Xie, J. Lian, F. Sun, B. Gan, Y. Wang, The lattice strain ratio in characterizing the grain-to-grain interaction effect and its specific insight on the plastic deformation of polycrystalline materials, The Journal of Strain Analysis for Engineering Design 53(5) (2018) 353-363.
[38] Q. Xie, R. Li, Y.D. Wang, R. Su, J. Lian, Y. Ren, W. Zheng, X. Zhou, Y. Wang, The in-depth residual strain heterogeneities due to an indentation and a laser shock peening for Ti-6Al-4V titanium alloy, Materials Science and Engineering: A 714 (2018) 140-145.
[39] Q. Xie, S. Gorti, J.J. Sidor, Y.G. An, Y.D. Wang, J. Lian, H. Lan, K. An, Grain orientation dependence of the Residual Lattice Strain in a Cold Rolled Interstitial-Free Steel, Steel Research International 89(3) (2018) 1700408.
[40] A. Brückner-Foit, X. Huang, Numerical simulation of micro-crack initiation of martensitic steel under fatigue loading, International Journal of Fatigue 28(9) (2006) 963-971.
[41] R. Prasannavenkatesan, C.P. Przybyla, N. Salajegheh, D. McDowell, Simulated extreme value fatigue sensitivity to inclusions and pores in martensitic gear steels, Engineering Fracture Mechanics 78(6) (2011) 1140-1155.
[42] K. Gillner, S. Münstermann, Numerically predicted high cycle fatigue properties through representative volume elements of the microstructure, International Journal of Fatigue 105 (2017) 219-234.
[43] K. Gillner, M. Henrich, S. Münstermann, Numerical study of inclusion parameters and their influence on fatigue lifetime, International Journal of Fatigue 111 (2018) 70-80.
[44] D. Brooksbank, K.W. Andrews, tessellated stresses associated with some inclusions in steel, Journal of the Iron and Steel Institute 207 (1969) 474-483.
[45] Y. Ma, Y. Cui, Study of the effect of sulfur contents on fracture toughness of railway wheel steels for high speed train, Acta Metallurgica Sinica 47(8) (2011) 978-983.
[46] G. Tarjus, P. Schaaf, J. Talbot, Random sequential addition: a distribution function approach, Journal of Statistical Physics 63(1/2) (1991) 167-202.
[47] D. Brooksbank, K. Andrews, Thermal expansion of some inclusions found in steels and relation to tessellated stresses, Journal of the Iron and Steel Institute 206(6) (1968) 595-599.
[48] C. Gu, J. Lian, Y. Bao, W. Xiao, S. Münstermann, Numerical Study of the Effect of Inclusions on the Residual Stress Distribution in High-Strength Martensitic Steels During Cooling, Applied Sciences 9(3) (2019) 455.
[49] F. Roters, P. Eisenlohr, L. Hantcherli, D.D. Tjahjanto, T.R. Bieler, D. Raabe, Overview of constitutive laws, kinematics, homogenization and multiscale methods in crystal plasticity finite-element modeling: Theory, experiments, applications, Acta Materialia 58(4) (2010) 1152-1211.
[50] J.R. Rice, Inelastic constitutive relations for solids: an internal-variable theory and its application to metal plasticity, Journal of the Mechanics and Physics of Solids 19(6) (1971) 433-455.

[51] C.O. Frederick, P.J. Armstrong, A mathematical representation of the multiaxial Bauschinger effect, Materials at High Temperatures 24(1) (2007) 1-26.
[52] C. Gu, Y.-P. Bao, P. Gan, J.-H. Lian, S. Münstermann, An experimental study on the impact of deoxidation methods on the fatigue properties of bearing steels, Steel Research International 89(9) (2018) 1800129.
[53] B.V. Molotilov, P.I. Yugov, Metallurgy of bearing steel, Steel in Translation 38(7) (2008) 565-568.
[54] C. Gu, J. Lian, Y. Bao, S. Münstermann, A microstructure sensitive modeling approach for fatigue life prediction considering the residual stress effect from heat treatment, Procedia Structural Integrity 13 (2018) 2048-2052.
[55] F. Fritzen, T. Böhlke, E. Schnack, Periodic three-dimensional mesh generation for crystalline aggregates based on Voronoi tessellations, Computational Mechanics 43(5) (2009) 701-713.
[56] G. Cailletaud, S. Forest, D. Jeulin, F. Feyel, I. Galliet, V. Mounoury, S. Quilici, Some elements of microstructural mechanics, Computational Materials Science 27 (2003) 351-374.
[57] G.R. Johnson, W.H. Cook, Fracture characteristics of three metals subjected to various strains, strain rates, temperatures and pressures, Engineering Fracture Mechanics 21(1) (1985) 31-48.
[58] Y. Bao, T. Wierzbicki, On fracture locus in the equivalent strain and stress triaxiality space, International Journal of Mechanical Sciences 46(1) (2004) 81-98.
[59] Y.L. Bai, T. Wierzbicki, A new model of metal plasticity and fracture with pressure and Lode dependence, International Journal of Plasticity 24(6) (2008) 1071-1096.
[60] J. Lian, M. Sharaf, F. Archie, S. Münstermann, A hybrid approach for modelling of plasticity and failure behaviour of advanced high-strength steel sheets, International Journal of Damage Mechanics 22(2) (2013) 188-218.
[61] H. Mughrabi, Dislocations in fatigue, Dislocations and properties of real materials, The Institute of Metals, London, 1984, pp. 244-262.
[62] A. Manonukul, F.P.E. Dunne, High- and low-cycle fatigue crack initiation, Proceedings of the Royal Society A: Mathematical, Physical and Engineering Sciences 460(2047) (2004) 1881-1903.
[63] K.-S. Cheong, E.P. Busso, Effects of lattice misorientations on strain heterogeneities in FCC polycrystals, Journal of the Mechanics and Physics of Solids 54(4) (2006) 671-689.
[64] H. Mughrabi, C. Wüthrich, Asymmetry of slip and shape changes during cyclic deformation of α-iron single crystals, The Philosophical Magazine: A Journal of Theoretical Experimental and Applied Physics 33(6) (1976) 963-984.
[65] C. Sommer, H. Mughrabi, D. Lochner, Influence of temperature and carbon content on the cyclic deformation and fatigue behaviour of α-iron. Part I. Cyclic deformation and stress–behaviour, Acta Materialia 46(5) (1998) 1527-1536.
[66] M. Boeff, H.u. Hassan, A. Hartmaier, Micromechanical modeling of fatigue crack initiation in polycrystals, Journal of Materials Research 32(23) (2017) 4375-4386.